Science
AAAS

Supplementary Materials for

An action potential initiation mechanism in distal axons for the control of dopamine release

Changliang Liu, Xintong Cai, Andreas Ritzau-Jost, Paul F. Kramer, Yulong Li, Zayd M. Khaliq, Stefan Hallermann, and Pascal S. Kaeser

Correspondence to: Changliang_Liu@hms.harvard.edu and kaeser@hms.harvard.edu

This PDF file includes:

Other Supplementary Materials for this manuscript include the following:

Materials and Methods

Mice

Animal experiments were approved by the Animal Care and Use Committees at Harvard University and at the National Institute of Neurological Disorders and Stroke (NINDS, NIH), and by the federal Saxonian Animal Welfare Committee, Germany, and were in accordance with the European (EU Directive 2010/63/EU, Annex IV for animal experiments) and the Leipzig University Guidelines. Mice were housed with free access to water and food, and males and females were used irrespective of sex in all experiments. Knock-in mice with Cre recombinase expression from the dopamine transporter (DAT) gene locus (denoted as $DAT^{IRES\text{-}Cre}$, RRID: IMSR_JAX:006660) (*42*) and the choline acetyltransferase (ChAT) gene locus (denoted as $ChAT^{IRES\text{-}Cre}$, RRID: IMSR_JAX:006410) (*43*) were used for cell type-specific manipulations of dopamine neurons or ACh neurons, respectively. For labeling vesicles in dopamine neurons or ACh neurons, a reporter line with a CAG promoter-driven loxP-STOP-loxP-synaptophysin-tdTomato cassette in the Rosa26 locus (SYP-$tdTomato^{LSL}$, RRID: IMSR_JAX:012570) was crossed with $DAT^{IRES\text{-}Cre}$ or $ChAT^{IRES\text{-}Cre}$ mice, respectively. For expression of ChR2 in dopamine neurons or ACh neurons, a knock-in line with a CAG promoter-driven loxP-STOP-loxP-ChR2-EYFP cassette in the Rosa26 locus (ChR2-$EYFP^{LSL}$, RRID: IMSR_JAX:012569) (*44*) was crossed to $DAT^{IRES\text{-}Cre}$ or $ChAT^{IRES\text{-}Cre}$ mice. For expressing eNpHR3.0 in ACh neurons, a knock-in line containing a CAG promoter-driven loxP-STOP-loxP-eNpHR3.0-EYFP cassette in the Rosa26 locus (eNpHR-$EYFP^{LSL}$, RRID: IMSR_JAX:014539) (*44*) was crossed with $ChAT^{IRES\text{-}Cre}$ mice. Simultaneous ablation of $Ca_V2.1$ and $Ca_V2.2$ proteins in dopamine neurons was achieved by crossing conditional *Cacna1a* knockout mice ($Ca_V2.1^{floxed}$) (*45*) with conditional *Cacna1b* knockout mice ($Ca_V2.2^{floxed}$, generated from KOMP CSD34514-1a-Wtsi) (*24*) and with $DAT^{IRES\text{-}Cre}$ mice. Deletion of $Ca_V2.3$ in dopamine neurons was achieved by crossing conditional *Cacna1e* knockout mice ($Ca_V2.3^{floxed}$) (*46*) to $DAT^{IRES\text{-}Cre}$ mice. In conditional knockout experiments, cKO^{DA} mice were mice with homozygous floxed Ca_V2 alleles and a heterozygous $DAT^{IRES\text{-}Cre}$ allele. Control mice were siblings of the corresponding cKO^{DA} mice, with

heterozygous floxed Ca_V2 alleles and a heterozygous $DAT^{IRES\text{-}Cre}$ allele.

Stereotaxic surgeries

Unless noted otherwise, surgeries were performed unilaterally and in the right hemisphere. Mice were anesthetized with 5% isoflurane and mounted in a stereotaxic frame. 1.5–2% isoflurane was used to maintain stable anesthesia during surgery. A small hole was drilled after exposing the skull, and the AAVs were injected through a microinjector (108 µm needle diameter) at coordinates described in each individual section with a rate of 0.1 µl/min for a total volume of 1 µl. The microinjector was left in place for 10 min to allow diffusion of the virus after injection. Following recovery from surgery, mice were returned to their home cage for at least 14 days before testing. Viruses were aliquoted, stored at - 80 °C, and diluted immediately before injection. Local lesion of dopamine axons was performed by microinjection of 2 µl 6-OHDA (25 mM in PBS) into the right striatum (coordinates: 1.0 mm anterior from Bregma, 2.0 mm lateral, and 3.3 mm below pia). Specific AAVs used during stereotaxic surgeries are listed below for each experiment.

Slice imaging

Adeno-associated viruses (AAVs) expressing $GRAB_{DA2m}$ (*13*), $rGRAB_{DA1h}$ (*13*), and $GRAB_{ACh3.0}$ (*15*) under a human synapsin 1 (hSyn) promoter (AAV9-hSyn-$GRAB_{DA2m}$, AAV9-hSyn-$rGRAB_{DA1h}$, and AAV9-hSyn-$GRAB_{ACh3.0}$, respectively) were purchased from WZ Biosciences, Inc. with permission from Y.L. For measuring dopamine and ACh release in slices, 1 µl AAV9-hSyn-$GRAB_{DA}$ (3–6 x 10^{12} copies/ml), AAV9-hSyn-$rGRAB_{DA}$ (3–6 x 10^{12} copies/ml), or AAV9-hSyn-$GRAB_{ACh}$ (4–8 x 10^{12} copies/ml) was injected into the midbrain (coordinates relative to Lambda: 1.1 mm anterior, 1.3 mm lateral and 4.2 mm below pia) at 45–77 days of age. 26–43 days after injection, the mice were deeply anesthetized with isoflurane and decapitated. Parasagittal mouse brain slices containing the striatum (250 µm thick unless noted otherwise) were cut using a vibratome (Leica, VT1200s) in an ice-cold cutting solution containing (in mM): 75 NaCl, 2.5 KCl, 7.5 $MgSO_4$, 75 Sucrose, 1 NaH_2PO_4, 12 Glucose, 26.2

$NaHCO_3$, 1 Myo-inositol, 3 Pyruvic acid, 1 Ascorbic acid. After cutting, slices were incubated at room temperature in an incubation solution containing (in mM): 126 NaCl, 2.5 KCl, 2 $CaCl_2$,1.3 $MgSO_4$, 1 NaH_2PO_4, 12 Glucose, 26.2 $NaHCO_3$, 1 Myo-inositol, 3 Pyruvic acid, 1 Ascorbic acid for at least 1 h before use. Recordings were performed in a recording chamber continuously perfused with artificial cerebrospinal fluid (ACSF) containing (in mM): 126 NaCl, 2.5 KCl, 2 $CaCl_2$, 1.3 $MgSO_4$, 1 NaH_2PO_4, 12 Glucose, 26.2 $NaHCO_3$ heated to 30–32 °C at 2.5–3 ml/min. All solutions were constantly bubbled with 95% O_2 and 5% CO_2, and all recordings were completed within 6 h after slicing. Fluorescence imaging was performed using an Olympus BX51 epifluorescence microscope. Fluorescent signals were excited with a 470 or 565 nm LED, collected through a 4X objective, and digitized with a scientific complementary metal-oxide-semiconductor camera (sCMOS, Hamamatsu Orca-Flash4.0). Spontaneous dopamine and ACh release were imaged at 512 x 512 pixels/frame, 10 frames/s, with an exposure time of 50 ms. Evoked responses were acquired at 512 x 512 pixels/frame, 50 frames/s, with an exposure time of 20 ms. Each pixel represents a physical area of 5.4 x 5.4 μm^2. For image analyses, regions of interest (ROIs) containing the striatum were manually selected in each image stack (1–3 min for spontaneous release), and the backgrounds were estimated from cortical regions where no sensor was expressed. After background subtraction, each frame was blurred by box filtering with a radius of 5 pixels. For detection of spontaneous release, a dynamic baseline fluorescence (F_0) was estimated for each pixel by smoothing the time course with a moving average over a 10-s sliding window for 10 times. A time course of $(F-F_0)/F_0$ (from hereon: $\Delta F/F_0$) was then calculated. Image stacks were binarized with a $\Delta F/F_0$ threshold > 0.005 and > 1 x standard deviation (SD) of the $\Delta F/F_0$ of the recording period for each pixel. The pixels above threshold were further filtered with a rise speed of $\Delta F/F_0 > 0.1\ s^{-1}$ and > 1 x SD of the rise speed for at least 1 frame during the positive periods. Release events were defined as clusters containing more than 20 adjacent pixels above threshold in every frame and more than 500 adjacent pixels above threshold in at least one frame with a total duration of 1.2–6 s for $GRAB_{DA}$ signals and 0.4–2 s for $GRAB_{ACh}$ signals (due to faster kinetics of $GRAB_{ACh}$) (*13*, *15*). Overlapping events were segregated using density-based spatial clustering with a radius of 25% of the raw cluster and a minimum duration of 1 s and 0.3 s for

$GRAB_{DA}$ and $GRAB_{ACh}$, respectively. The segregation process was iterated until no new event was generated. Frequency maps were generated by counting the number of events in each pixel during the recording period. For the quantification of evoked release, F_0 was estimated as the average fluorescence signal over 0.5 s immediately before stimulation. $\Delta F/F_0$ was then calculated for each pixel, and pixels with a $\Delta F/F_0 > 0.02$ in response to electrical stimulation were considered as part of a release event and used for further quantification. Example images in each experiment were contrast adjusted using identical settings. The number of dopamine terminals recruited during a dopamine release event was estimated as the product of the volume of the event (event area x thickness of slice) and the density of synaptophysin-tdTomato-labelled dopamine terminals in the striatum ($0.16/\mu m^3$, SYP-tdTomato^{LSL} x DAT$^{IRES\text{-}Cre}$ mice) (*14*).

Amperometry and field recordings

Carbon-fiber microelectrodes (CFE, 7 μm in diameter, 50–100 mm in length, Goodfellow) were fabricated in the laboratory and calibrated immediately before use by puffing dopamine solutions (*14*). The recording electrode was placed in the dorsal striatal slices prepared as described above, and held at a constant voltage of 600 mV for amperometry. Signals were amplified with a multiclamp 700B amplifier (Molecular Devices), low-pass filtered at 400 Hz, and digitized using a Digidata 1440A Digitizer (Molecular Devices). Electrical stimulation was carried out with a unipolar glass pipette (tip diameter of 3–5 μm) filled with ACSF. The electrode was placed 100–150 μm away from the CFE. The frequency, duration, and magnitude of the stimulus were controlled through a digitizer (1440A) and a linear stimulus isolator (A395, World Precision Instruments). A biphasic wave (0.25 ms in each phase) was applied for stimulation. For the activation of ChR2, brief pulses of light (470 nm; 1 ms duration; 7.5 mW/mm^2) were delivered at the recording site using an LED light source. Recordings in Fig. 2, C to E, were performed after blocking AMPA receptors (CNQX, 20 μM), NMDA receptors (APV, 50 μM), $GABA_A$ receptors (PTX, 50 μM), DAT (CGP55845, 0.1 μM), D2 receptors (sulpiride, 0.6 μM), and muscarinic AChRs (atropine, 2 μM). NpHR3.0 was activated using a 590 nm LED with an output power of 1.8 mW/mm^2.

Evoked field potentials (Fig. 3, A to C) were recorded using the same CFE in current-clamp mode without any current injection and low-pass filtered at 10 kHz. Local lesion of dopamine axons was done as described above, and recordings were performed 16–57 days after the surgery. The extent of the lesion was confirmed post hoc using immunostaining. The recorded slices were fixed with 4% paraformaldehyde (PFA) in PBS for 2 h, blocked in 10% goat serum in PBS, permeabilized in 0.25% Triton X-100 in PBS, stained with rabbit anti-VAChT (1:500, Sysy 139103) and guinea pig anti-TH (1:1,000, RRID: AB_2619897) for 12 h at 4 °C and secondary antibodies (tagged with Alexa 488 and 568) for 2 h at room temperature, mounted on #1.5 cover glasses (GG-18-1.5-pdl, neuVitro) using H-1000 mounting medium (Vectashield), and imaged using an Olympus FV1000 laser scanning confocal microscope.

Patch-clamp electrophysiology

Cell-attached recordings were performed in voltage-clamp mode using acute mouse brain slices prepared with the same method described in slice imaging (postnatal days 51–145). eNpHR3.0-EYFP was expressed in ACh neurons (eNpHR3.0-EYFP^{LSL} mice x ChAT$^{IRES\text{-}Cre}$ mice), and a glass pipette (2–3 μm in diameter) filled with ACSF was used for recording. After a gigaohm seal was established on an eNpHR3.0-EYFP expressing cell, the holding voltage was adjusted until there was no net flow of current through the pipette. Signals were amplified with a Multiclamp 700B amplifier (Molecular Devices), low-pass filtered at 2 kHz, and digitized using a Digidata 1440A Digitizer (Molecular Devices). Action potentials were detected with an amplitude threshold > 3 x SD of the recording and visually inspected afterwards. *Whole-cell axonal recordings* were performed in acute striatal slices from mice (postnatal days 122–181) with the expression of synaptophysin-tdTomato in dopamine neurons (SYP-tdTomato^{LSL} x DAT$^{IRES\text{-}Cre}$). Brain hemispheres mounted in a chamber filled with chilled ACSF were sliced parasagittally at 300 μm and kept in ACSF at 37 °C for 15 minutes. The slices were then transferred to ACSF at room temperature until testing. ACSF for slicing, slice retention and recordings contained (in mM): 125 NaCl, 3 KCl, 25 Glucose, 25 $NaHCO_3$, 1.25 Na_2HPO_4, 1.0 $MgCl_2$, 1.1 $CaCl_2$. For recordings,

brain slices were mounted on an upright two-photon laser scanning microscope (Femtonics) equipped with a pulsed Ti:Sapphire laser (MaiTai, SpectraPhysics) tuned to 1020 nm and a 60x/1.0 NA objective (Olympus). Whole-cell current-clamp recordings from dopamine axons in the dorsal striatum were performed with quartz pipettes (Heraeus Quartzglas), pulled by a modified DMZ Universal Electrode Puller with oxygen-hydrogen burner (Zeitz Instruments) to a resistance of 8–17 MΩ. Pipettes were filled with potassium gluconate–based internal solution containing (in mM): 150 K-gluconate, 3 Mg-ATP, 0.3 Na-GTP, 10 K-HEPES, 10 NaCl, and 0.2 EGTA, pH adjusted to 7.2 with KOH. Pipettes were fixed into a custom-built electrode holder mounted on a micromanipulator (Kleindiek Nanotechnik). All recordings were performed in continuously perfused ACSF heated to 34.0–36.5 °C. Membrane voltages were recorded with a Multiclamp 700A patch-clamp amplifier (Molecular Devices) and digitized and filtered (200 kHz and 3 kHz 8-pole Bessel filter, respectively) by a HEKA EPC10/2 amplifier running Patchmaster software (HEKA Elektronik). Pipette capacitances were determined in the cell-attached configuration in voltage-clamp mode by the automated, fast capacitance cancellation of the Multiclamp 700A. Upon establishing whole-cell configuration, the amplifier was changed to current-clamp mode, and pipette capacitance was canceled using the value determined in voltage-clamp as previously established for presynaptic recordings (*26*). Holding currents were adjusted to keep membrane potentials between -70 to -75 mV (not liquid-junction corrected). For stimulation of nAChRs on dopamine axons, a second pipette pulled from borosilicate glass (Science Products, tip opening diameters of 2–3 µm) was used to apply carbachol puffs (100 µM in ACSF with 40–100 µM Atto 488). Puffs (0.6–1.2 bar, 8–30 ms) were applied 20–40 µm away from the recording site at intervals of 10 s. The efflux of carbachol during puff application was inspected by continuous two-photon x-y scans of the fluorescence of Atto 488. The puff-increased Atto 488 fluorescence reached a diameter of 10–15 µm and dissipated within ~2 s. Recorded responses of each axon with action potential firing in response to carbachol puffs are shown (axon 1: Fig. 3J, axons 2 and 3: fig. S7F). For one of the recordings (axon 3), small sinusoidal functions were subtracted from the traces to remove a 50-Hz-electrical noise artifact in this experiment (amplitude 1 to 3 mV, frequency 50 Hz). Irresponsiveness of some axons to carbachol puffs is likely due to suboptimal

positioning of the puff pipette relative to nAChRs on dopamine axons. Because the whole-cell recordings from dopamine axons are fragile, limited in time and sensitive to movement of the puff pipette, repositioning of the puff pipette during recordings was not possible. *For perforated patch axonal recordings*, $DAT^{IRES\text{-}Cre}$ x $ChAT^{IRES\text{-}Cre}$ mice were used. For labeling dopamine axons, AAVs encoding a Cre-dependent double-floxed inverted open reading frame of tdTomato under a CAG promoter (AAV9-CAG-Flex-tdTomato, Penn Vector Core) were injected bilaterally into the substantia nigra (coordinates: 2.4 mm posterior from Bregma, 1.4 mm lateral and 5.2 mm below the skull). For expressing channelrhodopsin in cholinergic interneurons, AAVs encoding a Cre-dependent double-floxed inverted open reading frame of ChR2-EYFP under an Ef1a promoter (AAV5-Ef1a -Flex-ChR2-EYFP, 4 x 10^{12} copies/ml, UNC Vector Core; for 2 mice) or double-floxed inverted open reading frame of channelrhodopsin-GFP under a human synapsin 1 promoter (AAV1-hSyn-Flex-CoChR-GFP, 5.7 x 10^{12} copies/ml, UNC Vector Core; for 1 mouse) were injected bilaterally into the medial dorsal striatum (coordinates: 0.8 mm anterior from Bregma, 1.8 mm lateral and 3.3 mm below the skull). Recordings were performed on adult mice (postnatal days 119–133). Mice were anesthetized with isoflurane, decapitated, and brains were rapidly extracted. Horizontal sections were cut at 330 μm thickness on a vibratome while immersed in heated (34 °C), modified, slicing ACSF containing (in mM): 198 glycerol, 2.5 KCl, 1.2 NaH_2PO_4, 20 HEPES, 25 $NaHCO_3$,10 glucose, 10 $MgCl_2$, 0.5 $CaCl_2$, 5 Na-ascorbate, 3 Na-pyruvate, and 2 thiourea. Cut sections were removed from the slicing chamber and incubated for 30–60 minutes in a heated (34 °C) chamber with holding solution containing (in mM): 92 NaCl, 30 $NaHCO_3$, 1.2 NaH_2PO_4, 2.5 KCl, 35 glucose, 20 HEPES, 2 $MgCl_2$, 2 $CaCl_2$, 5 Na-ascorbate, 3 Na-pyruvate, and 2 thiourea. Slices were then stored at room temperature and used 30 min to 6 h later. Following incubation, slices were moved to a heated (33–35 °C) recording chamber that was continuously perfused with recording ACSF (in mM): 125 NaCl, 25 $NaHCO_3$, 1.25 NaH_2PO_4, 3.5 KCl, 10 glucose, 1 $MgCl_2$, 2 $CaCl_2$. Perforated-patch recordings were made using borosilicate pipettes (5–10 MΩ) filled with an internal solution containing (in mM): 135 KCl, 10 NaCl, 2 $MgCl_2$, 10 HEPES, 0.5 EGTA, 0.1 $CaCl_2$, adjusted to a pH value of 7.43 with KOH, 278 mOsm. Pipette tips were back-filled first with ~1 μl of internal solution

lacking gramicidin followed by internal solution containing 80–100 µg/ml gramicidin. Patch integrity was monitored by the addition of Alexa-488 to the gramicidin-containing internal solution. A white light LED (Thorlabs, SOLIS-3C) was used in combination with a tdTomato (Thorlabs, TLV-U-MF2-TOM) or EGFP (Chroma, 49002) filter set to visualize the dopamine axons (tdTomato) or excite the light-activated ion channel (EGFP). For opsin activation, the LED was controlled with a TTL pulse of 2–5 ms.

3D-SIM imaging

3D-SIM imaging was performed following previously described methods (*14*, *47*). Vesicles in ACh neurons were labeled by crossing SYP-tdTomato^{LSL} mice with ChAT$^{IRES\text{-}Cre}$ mice. ChAT$^{IRES\text{-}Cre}$ mice homozygote for SYP-tdTomato^{LSL} were deeply anesthetized with 5% isoflurane at postnatal days 64–75, perfused transcardially with 30 ml PBS at room temperature and 50 ml 4% PFA in PBS at 4 °C. Coronal slices (20 µm thick) containing striatum were cut using a vibratome (Leica, VT1000s) in ice-cold PBS. All slices were blocked in 10% goat serum in PBS, permeabilized in 0.25% Triton X-100 in PBS, stained with rabbit anti-TH (1:1,000, AB152, RRID: AB_390204) antibodies for 12 h at 4 °C and secondary antibodies (tagged with Alexa 488) for 2 h at room temperature, and mounted on #1.5 cover glasses (GG-18-1.5-pdl, neuVitro) using H-1000 mounting medium (Vectashield). 3D-SIM data were acquired with a DeltaVision OMX V4 Blaze microscope (GE Healthcare) equipped with a 60x/1.42 N.A. oil immersion objective and separate Edge 5.5 sCMOS cameras (PCO) for each channel. Z stacks were acquired with a z-step of 125 nm and 15 raw images per plane (five phases, three angles). Spherical aberrations were minimized using immersion oil matching. Superresolution images were computationally reconstructed from the raw datasets with a channel-specific measured optical transfer function and a Wiener filter constant of 0.002–0.003. Channel misregistration was measured using a control slide, and multi-channel datasets were registered. 3–5 ROIs were imaged from the dorsal striatum in each slice with imaging volumes of 40 x 40 x 2.5 µm^3. For analyses, ROIs (21.7 x 20.7 x 1 µm^3 – 36.3.7 x 37.4 x 2 µm^3) with a relatively even distribution of labeled terminals were manually selected in each image stack, and a custom MATLAB program described before (*14, 41*) was used to analyze the 3D datasets. Binary images in each

layer of the stack were first generated with the threshold determined by automatic two-dimensional segmentation (Otsu algorithm). Objects in each channel were recognized by the size of the cluster formed by contiguous voxels with a size filter of 0.04–2 μm^3. The minimal distance of each cholinergic nerve terminal from the nearest TH axon surface was calculated, and terminals with an overlap of > 0 voxels were considered contacting. Shuffled data were generated by randomly relocating cholinergic terminals within 5 x 5 x 1 μm^3. The effect of shuffling was evaluated by averaging 1,000 rounds of shuffling and distance quantification. Volume and surface rendering of the example images were generated from raw images stacks using Imaris (BITPLANE) with contrast adjusted using identical settings for all images.

In vivo fiber photometry

AAV9-hSyn-$GRAB_{DA2m}$ (2–3 x 10^{12} copies/ml) and AAV9-CAG-tdTomato (1–2 x 10^{12} copies/ml), or AAV9-hSyn-$GRAB_{ACh3.0}$ (2–3 x 10^{12} copies/ml) and AAV9-CAG-tdTomato (1–2 x 10^{12} copies/ml), or AAV9-hSyn-$GRAB_{ACh3.0}$ (2–3 x 10^{12} copies/ml) and AAV9-hSyn-$rGRAB_{DA1h}$ (2–3 x 10^{12} copies/ml) were co-injected into the right dorsal striatum (coordinates: 0.5 mm anterior from Bregma, 1.8 mm lateral and 2.2 mm below pia) of 50–92 day old mice. An optofluid cannula (400 μm in diameter, Doric) was implanted at the same location immediately after virus injection. The cannula was fixed on the skull using dental cement and two bone screws (1.17 mm in diameter, Fine Science Tools). Animals were kept in an inverted 12/12-h light/dark cycle, and experiments were carried out 18–43 days after the surgery during the dark phase of the cycle. The mouse was connected to a fiber optic (400 μm in diameter, Doric) and a drug delivery tube and placed in a round arena (43 cm in diameter) illuminated with infrared light (850 nm, 30 $\mu W/cm^2$). Fiber photometric recordings started 5 min after the mice were placed in the arena and lasted for 60 min for each session using a custom-built system. Photometry signals were converted by silicon photodiodes (SM1PD1A, Thorlabs), amplified by photodiode amplifiers (PDA200C, Thorlabs), and sampled at 10,000 Hz by a multifunction I/O card (PCIe-6321, National Instruments). 470 nm and 565 nm LEDs (Thorlabs) were alternatively turned on for 10 ms every 40 ms (25 Hz), and the output in each channel during each cycle was assessed by averaging the readout when the corresponding LED was

on. The light power at the fiber end was adjusted (40–160 µW for 470 nm and 10–60 µW for 565 nm) at the beginning of each experiment to keep the signal of the two channels at similar levels. Animal behavior was recorded using an sCMOS camera (Thorlabs) synchronized with fiber photometry acquisition through a TTL control at 25 frames/s. Sensory stimuli were carried out by light flashes (565 nm LED, 50 $\mu W/cm^2$) that illuminated the open field arena for 200 ms at random intervals of 100-600 s. Synchrony of image acquisition and photometry was calibrated and confirmed using light flashes. Drugs were locally delivered using a microinjection syringe pump (Harvard Apparatus) at a rate of 0.1 µl/min for a total volume of 1 µl. Half of the tested animals were treated with ACSF (in mM, 155 NaCl, 2.5 KCl, 1.2 $CaCl_2$, 1.2 $MgCl_2$, and 5 glucose) on the first day of the test and DHβE (50–100 µM in ACSF, Tocris) in the following test carried out 24–48 h after. The other half were treated with DHβE first and ACSF later. Haloperidol (2 mg/kg) was injected intraperitoneally in tests performed at least 24 h after completing the local drug infusion experiments. For analyses, F_0 was first estimated by low-pass filtering of the raw data at 0.01 Hz, and $\Delta F/F_0$ was then calculated. For behavioral analyses, the snout, ears, and tail base were tracked in the videos using DeepLabCut (50-layer ResNet-50) trained with 840 distinct frames extracted from multiple videos for 1.02 million training iterations (*48*). Only video frames with tracking confidence levels > 0.99 were included in further analyses, and frames 1 s before and 10 s after the light flashes were excluded from the analysis. Head orientation was determined by the direction from the middle point of the two ears to the snout. Snout velocity at time point t was calculated from the snout displacement between t - 1 and t + 1 frames. The relative angle of velocity and head orientation was then calculated for each time point. For assessing the relationships between photometry signals and behavior, velocities whose amplitude and angle appeared less than 4 times during a 60-min recording session were considered rare events and excluded from the analyses. Movement initiations were defined as transitions from a low mobility state (velocity amplitude < 2 x SD and 25 mm/s for at least 1 s) to a high mobility state (velocity amplitude > 2 x SD and 25 mm/s for at least 80 ms). For comparison of movement initiation in response to local drug infusion, the threshold was reduced to include low-amplitude movement initiations as transitions from velocity amplitude < 0.5 x SD and 25 mm/s for at least 400 ms to velocity amplitude >

0.5 x SD and 25 mm/s for at least 80 ms. $GRAB_{DA}$ transients during movement were defined as transients during which the amplitude of the snout velocity was above the average speed of the recording period and 25 mm/s. $GRAB_{DA}$ transients at rest were defined as transients during which the amplitude of the velocity was lower than mean – 0.2 x SD and 10 mm/s. For quantification of initiation time of $GRAB_{ACh}$ and $rGRAB_{DA}$ to light stimulation, responses that exhibited an increase of z-score > 0.5 within 200 ms following the start of light stimulation in both channels were selected. The initiation time was defined as the time point of the fastest increase in the signals within 400 ms immediately after the start of stimulation.

Statistics

Data are shown as mean ± SEM unless noted otherwise. Numbers of observations in each experiment were based on previous publications and on trial experiments. No statistical methods were used to predetermine sample sizes. The experimenter was blind to genotype while acquiring and analyzing data in Fig. 2, F to I, and fig. S5, C and D, and blind to the drug treatment condition during data analysis in Fig. 4, G to M, and fig. S11. Statistical significance was set at * $p < 0.05$, ** $p < 0.01$, and *** $p < 0.001$. For each experiment, the values and definitions of n are specified in the figure legends. Mann-Whitney rank-sum tests were used for Figs. 1H, 2I, 3M, 4D, 4F, 4K and 4L; figs S1F, S1G, S2A, S2B, S4F, S4J, S4L, S4N, S10C, S10F, S11D, S11E, and S11H. Wilcoxon signed-rank tests were used for Figs. 1E, 1G, 1K, 1L, 1O, 1P, 2E, and 4H; figs. S2, C to H, S3G, S4C, S4D, S4G, S4H, S8C, S11B, S11F, S11G, and S11I. Kruskal-Wallis analysis of variance with post hoc Dunn's tests were used for multigroup comparisons in Fig. 3F; figs. S1D, S1E, and S3D. Two-way ANOVA tests were performed for Fig. 2G, figs. S5D and S7E; a Kolmogorov-Smirnov test was used for Fig. 2B.

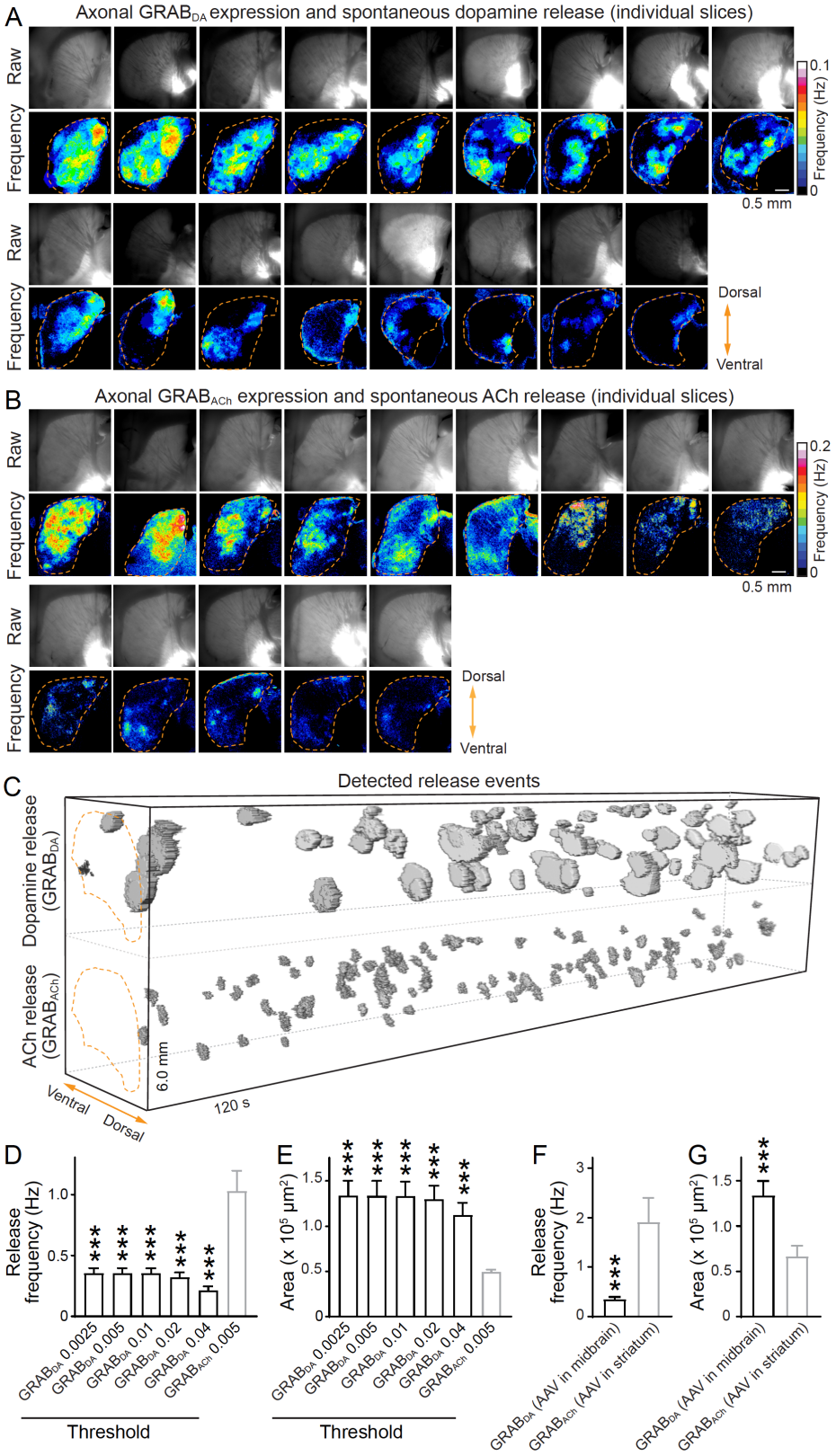

Fig. S1. Dopamine and ACh release measurements with fluorescent sensors. (**A**) Overview of

$GRAB_{DA}$ expression (top) and frequency map of spontaneous dopamine release (bottom) of each individual striatal slice of the experiment shown in Fig. 1, D and E. Dashed lines outline the striatum. Spontaneous dopamine release occurs in both the dorsal and ventral striatum and inhomogeneity in sensor expression does not explain the release patterns revealed by $GRAB_{DA}$ fluorescence changes. (**B**) As (A), but for spontaneous ACh release imaged via $GRAB_{ACh}$. (**C**) Volume-rendered dopamine (top) and ACh (bottom) release events detected via thresholding of fluorescence changes of $GRAB_{DA}$ and $GRAB_{ACh}$, respectively. Dopamine release appears less frequent but invades a larger area than ACh release. Experiments were done in different mice (expressing either $GRAB_{DA}$ or $GRAB_{ACh}$). (**D, E**) Quantification of frequency (D) and area (E) of release events detected with increasing thresholds for $GRAB_{DA}$ changes. Varying $GRAB_{DA}$ detection thresholds did not change the observations of lower frequency and larger area of $GRAB_{DA}$ events compared to $GRAB_{ACh}$ events; n = 17 slices/4 mice for $GRAB_{DA}$, 14/4 for $GRAB_{ACh}$. Original data identical to the data shown in Fig. 1, D to H, the threshold used for the experiments shown in Fig. 1, D to H, was 0.005 for both $GRAB_{DA}$ and $GRAB_{ACh}$. (**F, G**) Comparison of frequency (D) and area (E) of $GRAB_{DA}$ and $GRAB_{ACh}$ events in an experiment in which AAV-hSyn-$GRAB_{ACh}$ was injected into the striatum instead of the midbrain. Striatal $GRAB_{ACh}$ expression increased the frequency of detected events, but the $GRAB_{ACh}$ event area was still smaller than that of $GRAB_{DA}$. $GRAB_{DA}$ data are replotted from E with a threshold of 0.005; n = 17/4 for $GRAB_{DA}$, 8/3 for $GRAB_{ACh}$. Data are mean ± SEM; *** $p < 0.001$; Kruskal-Wallis analysis of variance with post hoc Dunn's tests for (D) and (E); Mann-Whitney rank-sum tests for (F) and (G).

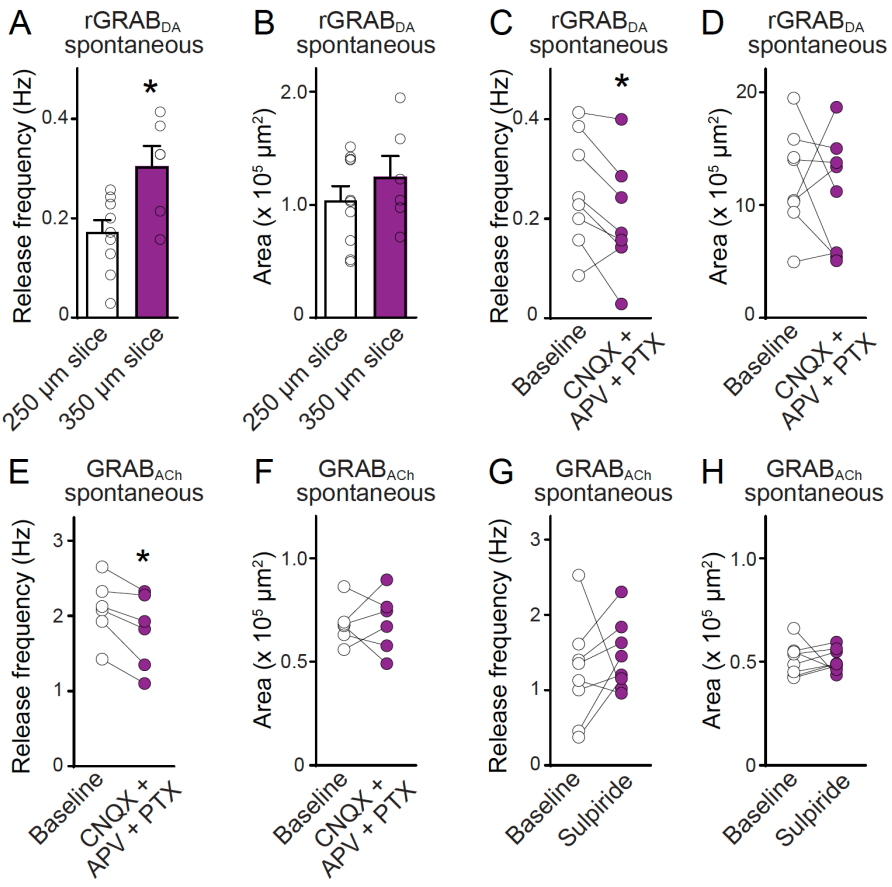

Fig. S2. Additional characteristics of spontaneous dopamine and ACh release. (**A, B**) Comparison of frequency (A) and area (B) of spontaneous dopamine release events detected using rGRAB$_{DA}$ in 250 or 350 µm thick slices. Higher frequency was detected in thicker slices; n = 10 slices/5 mice (250 µm), 6/5 (350 µm). (**C, D**) Quantification of frequency (C) and area (D) of dopamine release events before and after blocking AMPA receptors (CNQX, 20 µM), NMDA receptors (APV, 50 µM), and GABA$_A$ receptors (PTX, 50 µM); n = 8/3. (**E, F**) As (C, D), but for ACh release detected via GRAB$_{ACh}$; n = 6/3. (**G, H**) As (E, F), but before and after blocking D2 receptors with 0.6 µM sulpiride; n = 8/3. The increased frequency of GRAB$_{DA}$ events in thicker slices and relative insensitivity to blockers of synaptic transmission suggest that the spontaneous dopamine release is most likely caused by coincidence of pacemaker firing of cholinergic interneurons. Data are mean ± SEM; * $p < 0.05$; Mann-Whitney rank-sum tests for (A) and (B); Wilcoxon signed-rank tests for (C) to (H).

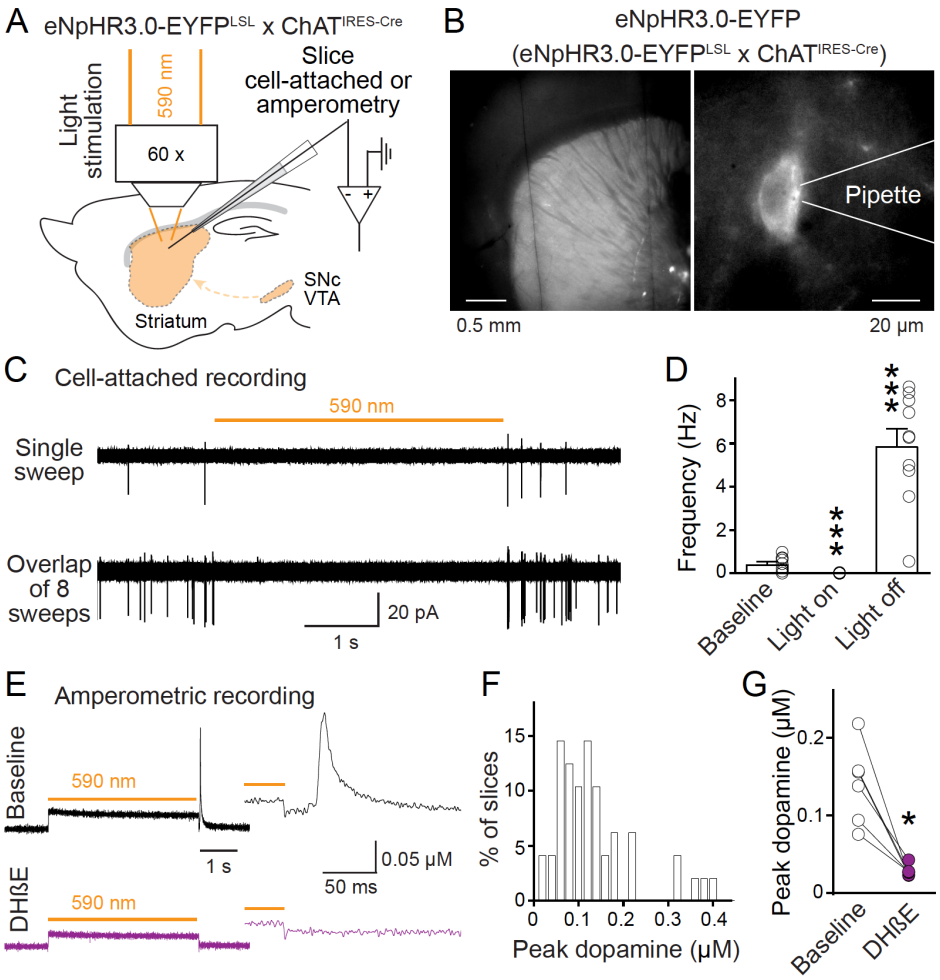

Fig. S3. Pause-rebound activity of ACh neurons induces dopamine release. (**A**) Strategy for mimicking the pause-rebound activity of ACh neurons. eNpHR3.0 was expressed using mouse genetics in ACh neurons. A 590 nm light pulse was used for silencing the firing of ACh neurons, and cell-attached recordings from ACh neurons or amperometry for dopamine were performed. (**B**) Example images of eNpHR3.0-EYFP expression in the striatum (left) and cell-attached recording from an ACh neuron (right). (**C**) Example traces of cell-attached recording of an ACh neuron in response to 4-s 590 nm LED light pulses. The light pulse suppressed spontaneous ACh neuron firing, and turning off this inhibition induced transient activity. (**D**) Quantification of firing frequencies before, during, and immediately after (0–200 ms) the light pulses; n = 10 cells/5 mice. (**E to G**) Example traces (E) and quantification (F and G) of amperometric recordings of dopamine release during the pause-rebound experiment, before and after

blocking nAChRs with 1 μM DHβE. Immediately after relieving the light-mediated inhibition, DHβE-sensitive dopamine transients were detected. (F) shows the frequency distribution of the peak of dopamine transients 0–200 ms after the light pulse, and (G) shows peak dopamine levels; F, n = 48 slices/7 mice; G, n = 6/4. Data are mean ± SEM; *** $p < 0.001$, * $p < 0.05$; Kruskal-Wallis analysis of variance with post hoc Dunn's test for (D); Wilcoxon signed-rank test for (G).

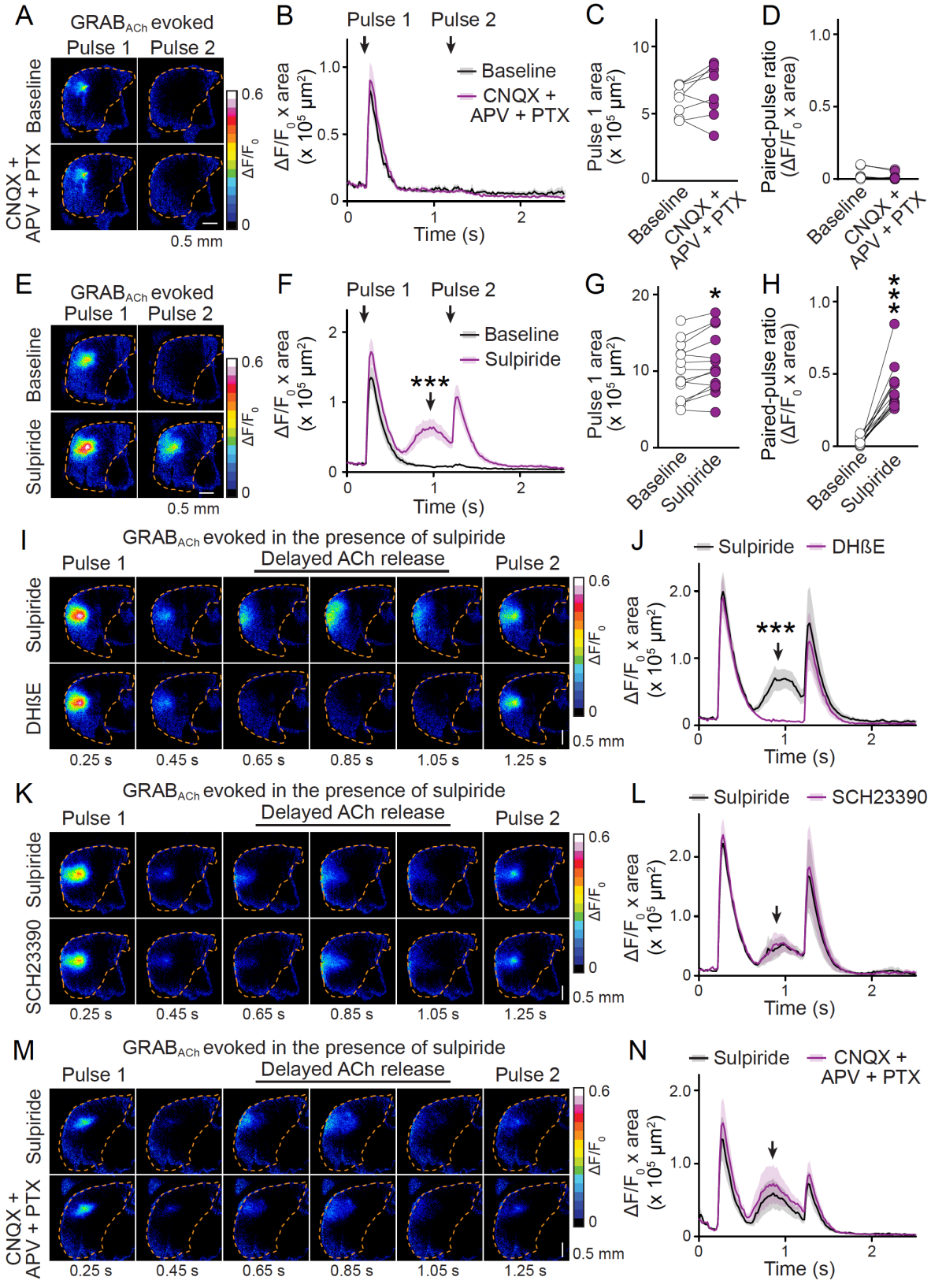

Fig. S4. D2 receptor-mediated feedback inhibition of ACh release. (**A to D**) Example images (A) and

quantification (B to D) of $GRAB_{ACh}$ signals evoked by paired electrical stimuli with an interval of 1 s before and after the blockade of AMPA receptors (CNQX, 20 μM), NMDA receptors (APV, 50 μM), and $GABA_A$ receptors (PTX, 50 μM). No significant change was detected; n = 8 slices/3 mice. (**E to H**) Similar to A to D, but showing the effects of blocking D2 receptors with 0.6 μM sulpiride. D2 inhibition enhanced $GRAB_{ACh}$ signals to both stimuli and induced an additional delayed phase (black arrow) of ACh release in response to the first stimulus that peaked at ~600–800 ms after stimulation; n = 14/4. (**I, J**) Example images (I) and quantification (J) of the additional delayed ACh release in the presence of 0.6 μM sulpiride before and after blockade of nAChRs with 1 μM DHβE. The delayed ACh release was abolished by DHβE, suggesting that it is caused by feedback mechanisms that involve nAChRs; n = 8/3. (**K to N**) As (I, J), but for blockade of D1 receptors with 1 μM SCH23390 (K, L) or AMPA receptors with 20 μM CNQX, NMDA receptors with 50 μM APV, and $GABA_A$ receptors with 50 μM PTX (M, N). No significant change in the delayed ACh release was seen; n = 6/3 each. Data are mean ± SEM; *** $p < 0.001$, * $p < 0.05$; Wilcoxon signed-rank tests for (C), (D), (G), and (H); Mann-Whitney rank-sum tests for areas under the curve (600–1200 ms) in (F), (J), (L), and (N).

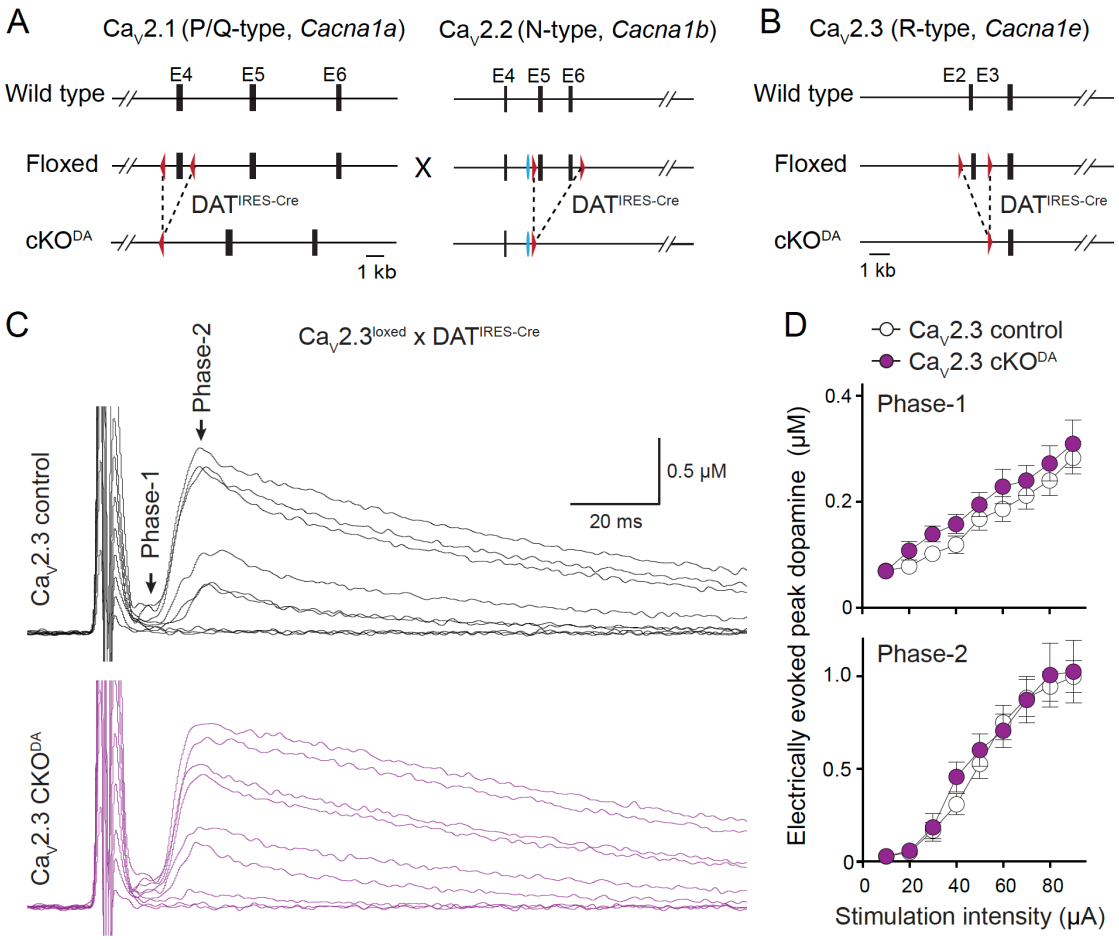

Fig. S5. Strategies for Ca_V2 ablation from dopamine neurons, and assessment of roles of $Ca_V2.3$ in dopamine release. (**A**) Simultaneous ablation of $Ca_V2.1$ and $Ca_V2.2$ from dopamine neurons by crossing conditional *Cacna1a* ($Ca_V2.1^{floxed}$) and *Cacna1b* ($Ca_V2.2^{floxed}$) knockout mice with $DAT^{IRES\text{-}Cre}$ mice. (**B**) Ablation of $Ca_V2.3$ from dopamine neurons by crossing conditional *Cacna1e* mice ($Ca_V2.3^{floxed}$) to $DAT^{IRES\text{-}Cre}$ mice. (**C, D**) Example traces (C) and quantification of peak amplitudes (D) of dopamine release evoked by electrical stimulation in mice in which $Ca_V2.3$ was ablated in dopamine neurons ($Ca_V2.3$ cKO^{DA}) and sibling control mice ($Ca_V2.3$ control). Phase-1 dopamine release was measured as the peak response within 10 ms after the stimulation, and phase-2 dopamine release was assessed as additional release after phase-1; n = 12 slices/4 mice for $Ca_V2.3$ control, 10/4 for $Ca_V2.3$ cKO^{DA}. $p > 0.05$ for genotype, stimulation intensity and interaction; two-way ANOVA. Data are mean ± SEM.

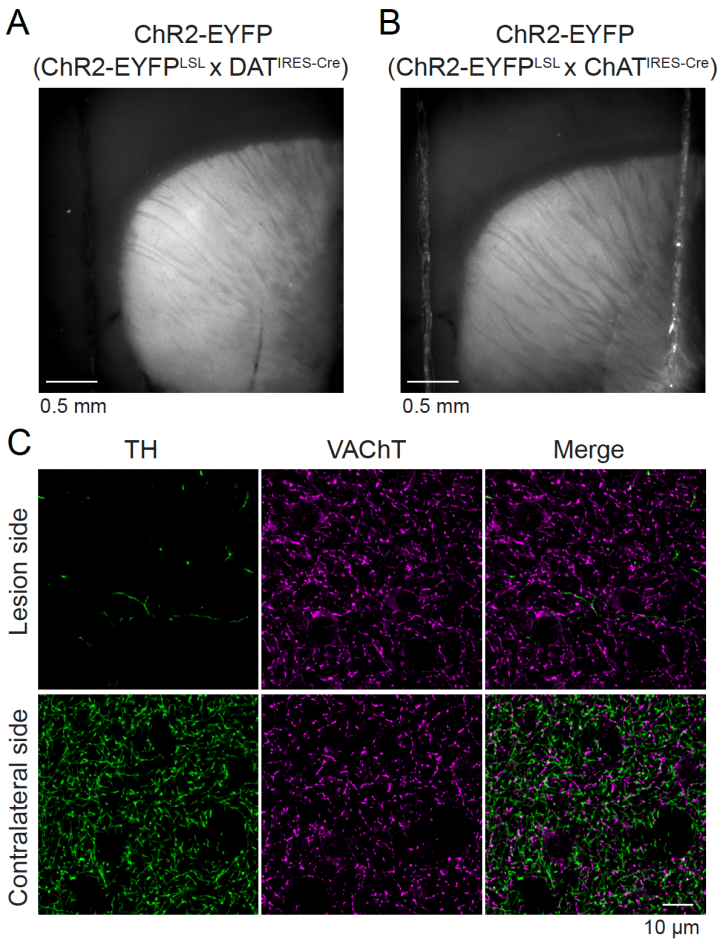

Fig. S6. ChR2-EYFP expression and 6-OHDA lesions. (**A, B**) Example images of sagittal striatal slices showing the distribution of ChR2-EYFP expressed in dopamine axons (A, crossing ChR2-EYFP^{LSL} mice to DAT$^{IRES-Cre}$ mice) and ACh neurons (B, crossing ChR2-EYFP^{LSL} mice to ChAT$^{IRES-Cre}$ mice). (**C**) Example confocal images of coronal striatal slices of TH and VAChT antibody staining in the lesioned and control sides of a mouse after unilateral 6-OHDA injection into the striatum. 6-OHDA lesion resulted in a loss of dopamine axons at the injection site but left cholinergic terminals intact.

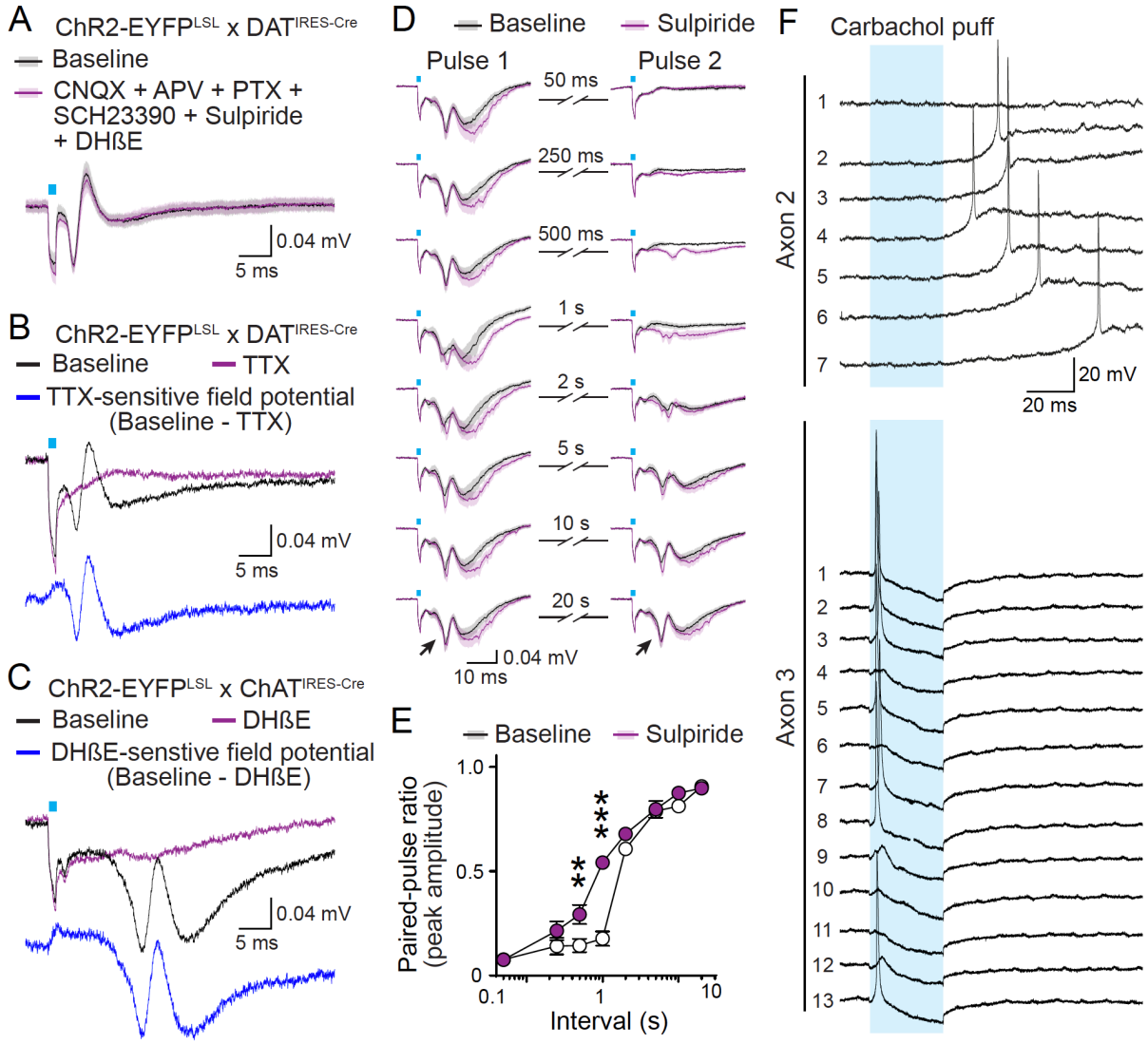

Fig. S7. Additional analyses of ACh-induced field potentials and carbachol-induced action potentials. (**A**) Average traces of light-evoked field potentials in mice expressing ChR2-EYFP in dopamine neurons, before and after the blockade of AMPA receptors (CNQX, 20 µM), NMDA receptors (APV, 50 µM), $GABA_A$ receptors (PTX, 50 µM), D1 receptors (SCH23390, 1 µM), D2 receptors (Sulpiride, 0.6 µM), and nAChRs (DHβE, 1 µM); n = 5 slices/1 mouse. (**B**) Example traces of field potential recordings (average of 4 sweeps from a single slice) before and after the application of 1 µM TTX, mice used in this experiment express ChR2-EYFP in dopamine axons. The TTX-sensitive field potential was obtained by subtracting the leftover signal in the presence of TTX from the baseline. (**C**) As (B), but for application of 1 µM DHβE in mice that express ChR2-EYFP in ACh neurons. (**D**) Average

traces of field potentials in response to paired-pulse stimulation using light (blue bar) with increasing interstimulus intervals before and after blocking D2 receptors with 0.6 μM sulpiride in mice expressing ChR2-EYFP in ACh neurons; n = 8/3. (**E**) Quantification of the paired-pulse ratios of the peak potential 5–15 ms after stimulation, arrows in bottom traces in (D). D2 receptor blockade significantly increased the amplitude of field potentials in response to the second stimulus when intervals were shorter than 2 s. These data indicate that the full depression of ACh-induced dopamine release during repetitive stimulation (Fig. 1, I to L) is caused mainly by dopamine feedback that reduces the capacity of ACh to induce firing in dopamine axons; n = 8/3; $p < 0.001$ for treatment, stimulation interval, and interaction; two-way ANOVA with post hoc Bonferroni test. (**F**) Example responses of dopamine axons 2 and 3 (axon 1 is shown in Fig. 3J) to carbachol puffs (100 μM, 10-s intervals). Carbachol puffing induced action potential firing in 3 of 14 recorded axons, likely because in many cases the positioning of the carbachol puff pipette was too distant from axonal nAChRs. The apparent hyperpolarization that follows the action potential in axon 3 is most likely an artifact caused by the puff or other mechanical movement. The variable delay in response to puffs is not dominated by action potential conduction velocities, but instead likely related to the positioning of the puff pipette, the opening of nAChRs, and charging and depolarizing the dopamine axonal membrane before action potential induction in dopamine axons. Similarly, in the optogenetic activation experiment shown in Fig. 3L, the ~10-ms delay is mainly due to the time it takes to sufficiently depolarize the axonal membrane. Data are mean ± SEM. *** $p < 0.001$, ** $p < 0.01$.

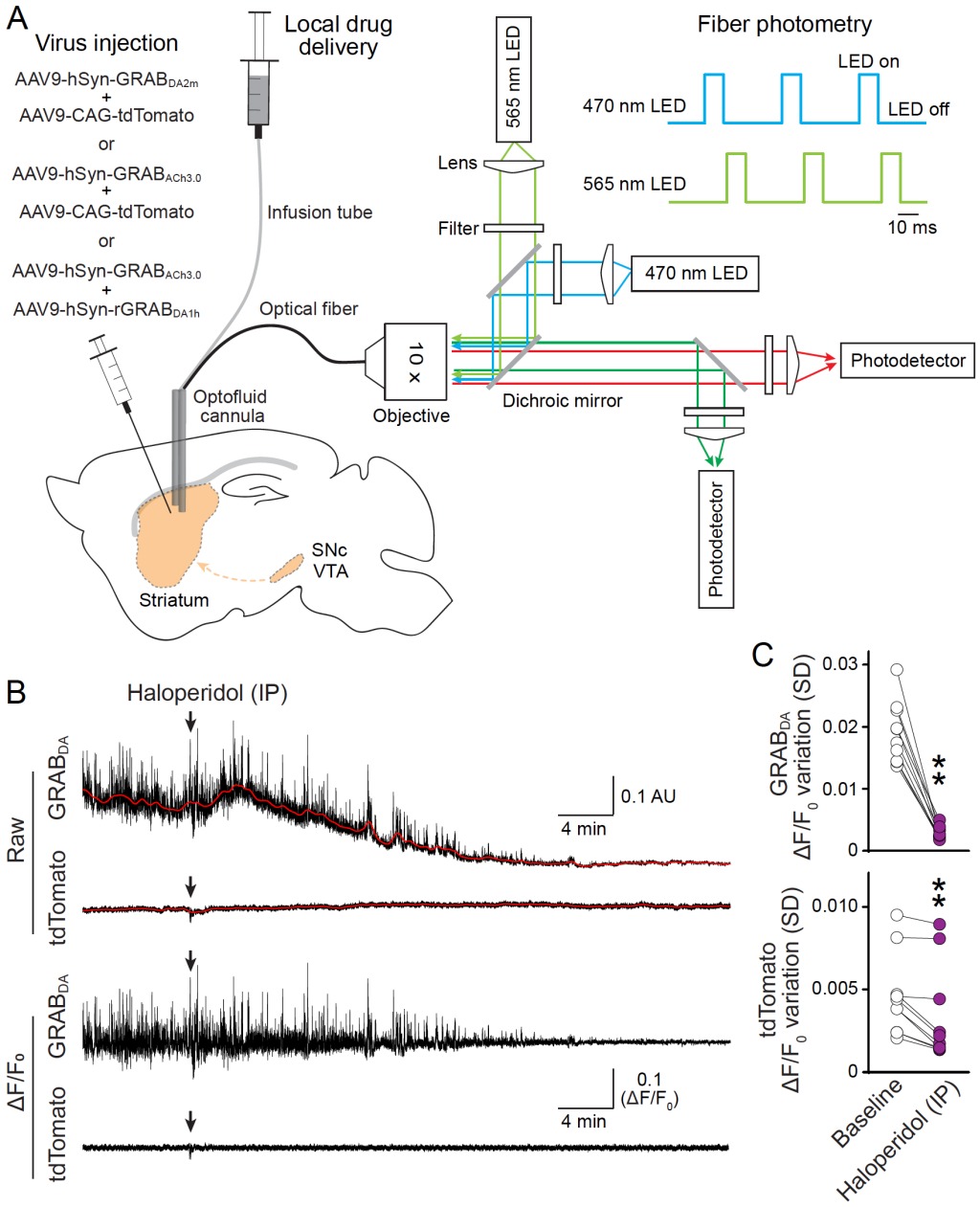

Fig. S8. Fiber photometry and drug delivery. (**A**) Schematic of AAV injection, photometry, and local drug delivery. AAVs were injected, and an optofluid cannula was implanted in the dorsal striatum of the right hemisphere in the same surgery. Photometry signals were acquired at 25 Hz with alternating illumination with 470-nm and 565-nm LEDs for 10 ms each in every 40-ms cycle. GRAB$_{DA}$ or GRAB$_{ACh}$ signals were only acquired when 470-nm LED was on, and the tdTomato or rGRAB$_{DA}$ signals were only acquired when the 565-nm LED was on. Local application of DHβE (50–100 μM) and ACSF were

carried out using a microinjection pump at a speed of 0.1 µl/min for 10 min. (**B**) Example recordings (top) and $\Delta F/F_0$ (bottom) of $GRAB_{DA}$ and tdTomato signals before and after intraperitoneal injection of the D2 receptor antagonist haloperidol (2 mg/kg, arrows). F_0 was estimated by low-pass filtering of the raw data at 0.01 Hz (red line). (**C**) Quantification of $GRAB_{DA}$ and tdTomato fluctuations (standard deviation of $\Delta F/F_0$) before and after intraperitoneal (IP) injection of haloperidol (2 mg/kg, arrows). Haloperidol abolished $GRAB_{DA}$ fluctuations. There is also a small but significant reduction in tdTomato fluctuations, most likely due to photobleaching and reduced movement in response to haloperidol; n = 10 mice. Data are mean ± SEM; ** $p < 0.01$; Wilcoxon signed-rank test for (C).

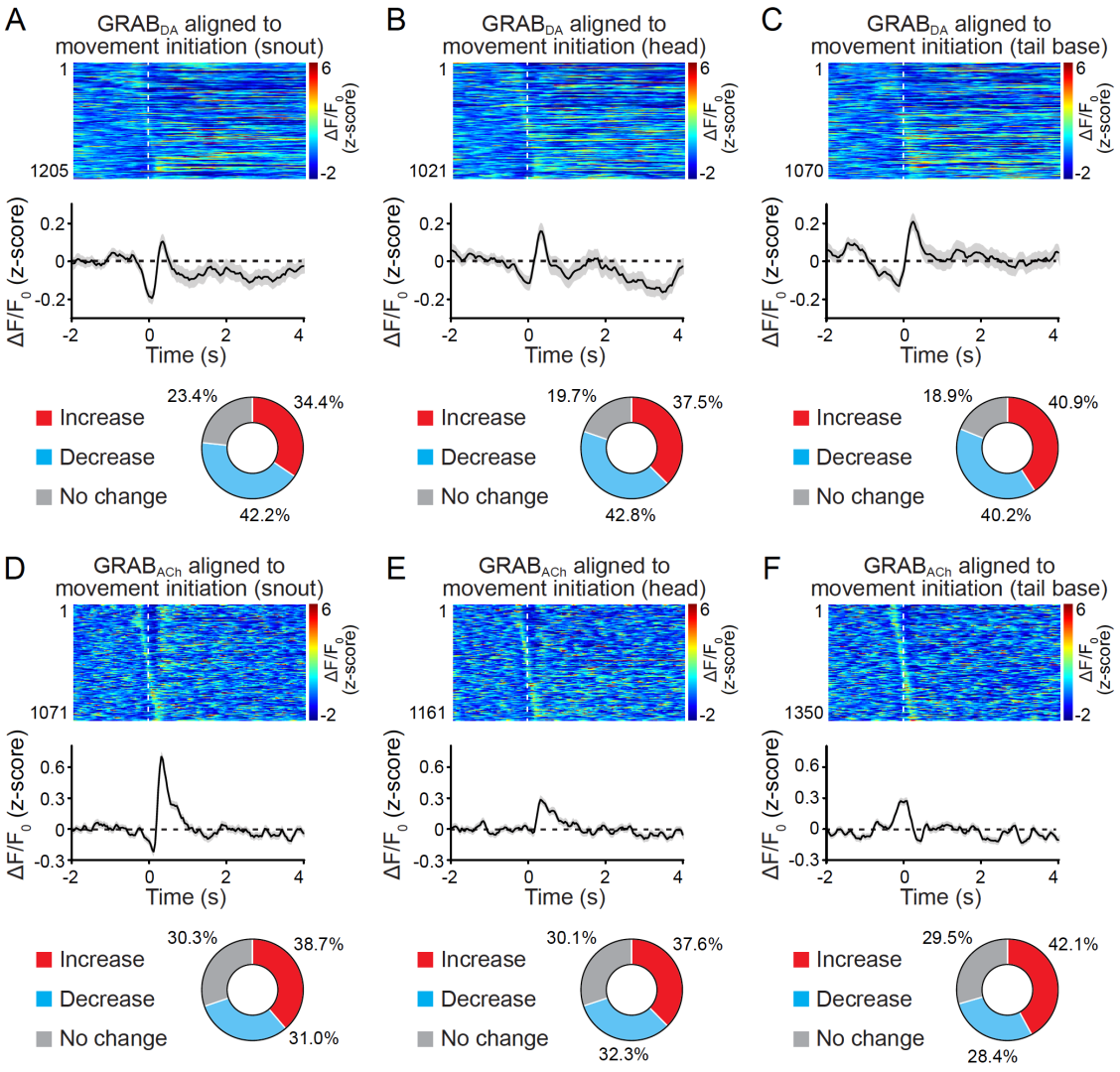

Fig. S9. Heterogeneity in GRAB$_{DA}$ and GRAB$_{ACh}$ dynamics during movement initiation. (**A to C**) Individual (top, heatmap, sorted by peak time), average (middle), and grouped (bottom) GRAB$_{DA}$ signals aligned to movement initiation (dashed line) based on the snout (A), the head (B, the center point between snout and ears), or the tail base (C). A response was considered an increase or a decrease when the z-score of the fluorescence change, assessed by the area ranging from 400 ms before to 400 ms after the movement initiation, was above 0.2 or below - 0.2, respectively. GRAB$_{DA}$ signals exhibit strong heterogeneity during movement initiation regardless of the body part used for movement analysis, illustrating that other factors or uncharacterized dimensions of movement contribute to striatal dopamine and ACh dynamics; A, n = 1205 events/10 mice; B, 1021/10, C, 1070/10 (C). (**D to F**) As A to C, but for

$GRAB_{ACh}$. Heterogeneity also exists in $GRAB_{ACh}$ signals during movement initiation; D, n = 1071/11; E, 1161/11; F, 1350/11. Data are mean ± SEM.

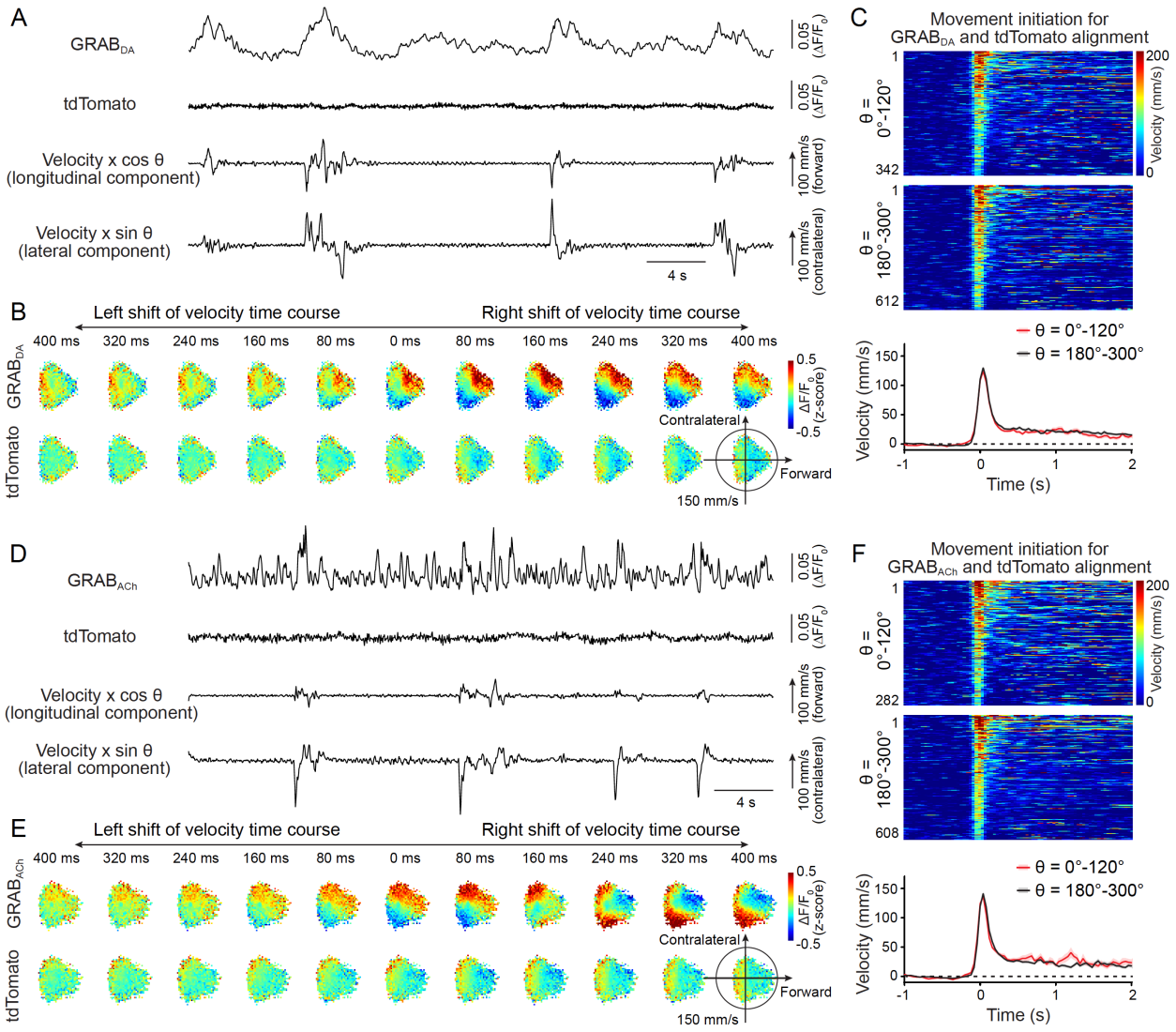

Fig. S10. Striatal dopamine and ACh levels are correlated with movement direction. (**A**) Example traces of GRAB$_{DA}$, tdTomato, and snout velocity. The velocity was decomposed as longitudinal and lateral components, and forward and contralateral directions were defined as positive directions in movement analyses. (**B**) Average GRAB$_{DA}$ and tdTomato signals registered to the artificially shifted velocity in polar coordinates. Stronger correlations between GRAB$_{DA}$ and movement direction were observed when the velocity time series was right-shifted, indicating that movement precedes GRAB$_{DA}$ peaks; n = 10 mice. (**C**) Individual (top, heatmap) and average (bottom) time courses of velocity amplitude during movement initiations used for the alignment of GRAB$_{DA}$ and tdTomato fluorescence. The average velocity amplitude before movement onset (40–1000 ms before the onset) was subtracted

before plotting; n = 342 events/10 mice for θ = 0º–120º, 612/10 for θ = 180º–300º. (**D to F**) As A to C, but for $GRAB_{ACh}$ signals. $GRAB_{ACh}$ exhibited a stronger correlation with movement direction when the velocity time series was right-shifted, and the relationship was inverted when the shift exceeded 320 ms (Fig. 4F); n = 282/11 for θ = 0º–120º, 608/11 for θ = 180º–300º. Data are mean ± SEM; Mann-Whitney rank-sum test for areas under the curve (0–400 ms) in (C) and (F).

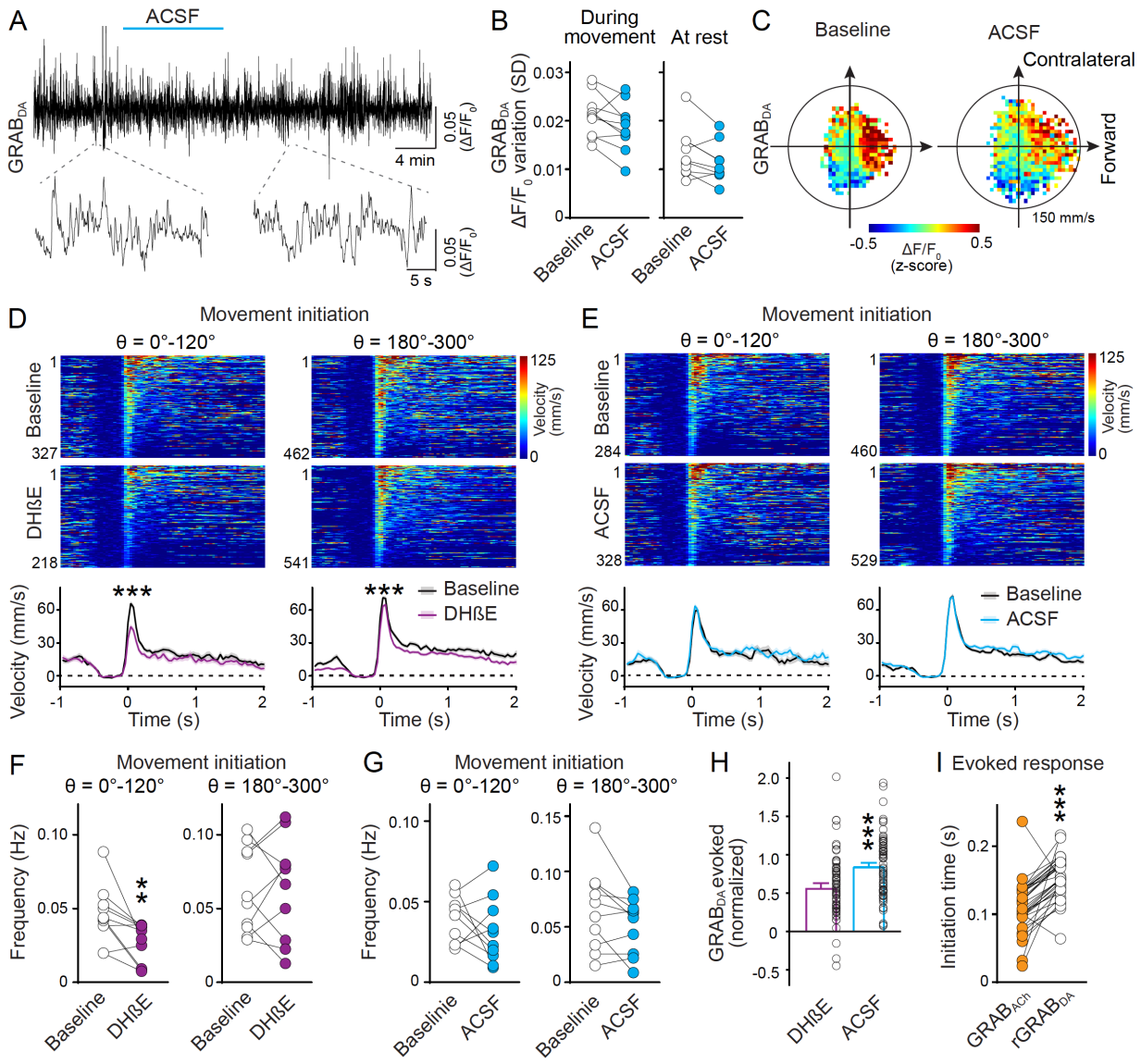

Fig. S11. Local inhibition of nAChRs in the striatum reduces movement initiation towards the contralateral side. (**A, B**) Example trace (A) and quantification (B, standard deviation, SD, of $\Delta F/F_0$) of $GRAB_{DA}$ fluorescence variation before and after local delivery of ACSF (1 µl) to the recording site via the optofluid canula. Despite the apparent tendency towards a reduced variation, no significant change was detected; n = 10 mice. (**C**) Average $GRAB_{DA}$ signals registered to the concurrent velocity in polar coordinates before and after ACSF application; n = 10. (**D**) Individual (top, heatmap) and average (bottom) time course of velocity amplitude during movement initiations before and after local infusion of DHβE into the right dorsal striatum at the recording site. Basal levels of velocity amplitude (40-400 ms

before the onset) were subtracted before plotting. DHβE infusion caused a significant reduction in the velocity amplitude of movement initiations with both θ = 0º–120º and θ = 180º–300º; n = 327 events/10 mice for baseline, 218/10 for DHβE with θ = 0º–120º; 462/10 for baseline, 541/10 for DHβE with θ = 180º–300º. (**E**) As (D), but for local infusion of ACSF. ACSF infusion caused no change in the velocity amplitudes in either direction; n = 284/11 for baseline, 328/11 for ACSF with θ = 0º–120º; 460/11 for baseline, 529/11 for ACSF with θ = 180º–300º. (**F**) Effects of DHβE on the frequency of movement initiations. DHβE reduced the frequency of movement initiations within θ = 0º–120º but not θ = 180º–300º; n = 10 mice each. (**G**) As F, but for local infusion of ACSF. No significant change was observed in the frequency of movement initiations in either direction; n = 10. (**H**) Comparison of relative changes in light-evoked $GRAB_{DA}$ responses after local infusion of DHβE or ACSF; n = 66 responses/10 mice for DHβE, 72/10 for ACSF. (**I**) Comparison of initiation times (time point for the fastest rise within 400 ms after the start of the stimulation) in light-evoked responses of simultaneously recorded $rGRAB_{DA}$ and $GRAB_{ACh}$ fluorescence changes in the dorsal striatum. Only responses that exhibited an increase of z-score > 0.5 within 200 ms following the start of the light stimulus were included in the analyses. $GRAB_{ACh}$ responses preceded those of $rGRAB_{DA}$; n = 34 responses/4 mice. Data are mean ± SEM; *** $p < 0.001$, ** $p < 0.01$; Mann-Whitney rank-sum tests for areas under the curve (0–400 ms) for (D), (E), and (H); Wilcoxon signed-rank tests for (B), (F), (G), and (I).

Movie S1. Spontaneous dopamine release in striatal slices. Example imaging and analyses of $GRAB_{DA}$ fluorescence in striatal slices (10 s, normal playback speed). A raw movie is shown on the left, the corresponding $\Delta F/F_0$ is shown in the middle, and detected dopamine release events are depicted on the right.

Movie S2. Spontaneous ACh release in striatal slices. Example imaging and analyses of $GRAB_{ACh}$ fluorescence in striatal slices (10 s, normal playback speed). A raw movie is shown on the left, the corresponding $\Delta F/F_0$ is shown in the middle, and detected dopamine release events are depicted on the right.

References and Notes

1. W. Matsuda, T. Furuta, K. C. Nakamura, H. Hioki, F. Fujiyama, R. Arai, T. Kaneko, Single nigrostriatal dopaminergic neurons form widely spread and highly dense axonal arborizations in the neostriatum. *J. Neurosci.* **29**, 444–53 (2009).
2. J. D. Berke, What does dopamine mean? *Nat. Neurosci.* **21** (2018), pp. 787–793.
3. C. Liu, P. Goel, P. S. Kaeser, Spatial and temporal scales of dopamine transmission. *Nat. Rev. Neurosci.* **22**, 345–358 (2021).
4. E. S. Bromberg-Martin, M. Matsumoto, O. Hikosaka, Dopamine in motivational control: rewarding, aversive, and alerting. *Neuron*. **68**, 815–34 (2010).
5. C. J. Wilson, The Mechanism of Intrinsic Amplification of Hyperpolarizations and Spontaneous Bursting in Striatal Cholinergic Interneurons. *Neuron*. **45**, 575–585 (2005).
6. S. Threlfell, T. Lalic, N. J. Platt, K. a. Jennings, K. Deisseroth, S. J. Cragg, Striatal dopamine release is triggered by synchronized activity in cholinergic interneurons. *Neuron*. **75**, 58–64 (2012).
7. N. Le Novère, M. Zoli, J. P. Changeux, Neuronal nicotinic receptor alpha 6 subunit mRNA is selectively concentrated in catecholaminergic nuclei of the rat brain. *Eur. J. Neurosci.* **8**, 2428–39 (1996).
8. I. W. Jones, J. P. Bolam, S. Wonnacott, Presynaptic localisation of the nicotinic acetylcholine receptor beta2 subunit immunoreactivity in rat nigrostriatal dopaminergic neurones. *J. Comp. Neurol.* **439**, 235–47 (2001).
9. M. F. Giorguieff, M. L. Le Floc'h, J. Glowinski, M. J. Besson, Involvement of cholinergic presynaptic receptors of nicotinic and muscarinic types in the control of the spontaneous release of dopamine from striatal dopaminergic terminals in the rat. *J. Pharmacol. Exp. Ther.* **200**, 535–44 (1977).
10. F.-M. Zhou, Y. Liang, J. A. Dani, Endogenous nicotinic cholinergic activity regulates dopamine release in the striatum. *Nat. Neurosci.* **4**, 1224–1229 (2001).
11. R. Cachope, Y. Mateo, B. N. Mathur, J. Irving, H.-L. Wang, M. Morales, D. M. Lovinger, J. F.

Cheer, Selective Activation of Cholinergic Interneurons Enhances Accumbal Phasic Dopamine Release: Setting the Tone for Reward Processing. *Cell Rep.* **2**, 33–41 (2012).

12. L. Wang, X. Zhang, H. Xu, L. Zhou, R. Jiao, W. Liu, F. Zhu, X. Kang, B. Liu, S. Teng, Q. Wu, M. Li, H. Dou, P. Zuo, C. Wang, S. Wang, Z. Zhou, Temporal components of cholinergic terminal to dopaminergic terminal transmission in dorsal striatum slices of mice. *J. Physiol.* **592**, 3559–3576 (2014).
13. F. Sun, J. Zhou, B. Dai, T. Qian, J. Zeng, X. Li, Y. Zhuo, Y. Zhang, Y. Wang, C. Qian, K. Tan, J. Feng, H. Dong, D. Lin, G. Cui, Y. Li, Next-generation GRAB sensors for monitoring dopaminergic activity in vivo. *Nat. Methods*. **17**, 1156–1166 (2020).
14. C. Liu, L. Kershberg, J. Wang, S. Schneeberger, P. S. Kaeser, Dopamine Secretion Is Mediated by Sparse Active Zone-like Release Sites. *Cell*. **172**, 706-718.e15 (2018).
15. M. Jing, Y. Li, J. Zeng, P. Huang, M. Skirzewski, O. Kljakic, W. Peng, T. Qian, K. Tan, J. Zou, S. Trinh, R. Wu, S. Zhang, S. Pan, S. A. Hires, M. Xu, H. Li, L. M. Saksida, V. F. Prado, T. J. Bussey, M. A. M. Prado, L. Chen, H. Cheng, Y. Li, An optimized acetylcholine sensor for monitoring in vivo cholinergic activity. *Nat. Methods*. **17**, 1139–1146 (2020).
16. A. A. Mamaligas, C. P. Ford, Spontaneous Synaptic Activation of Muscarinic Receptors by Striatal Cholinergic Neuron Firing. *Neuron*. **91**, 574–586 (2016).
17. J. M. Schulz, M. J. Oswald, J. N. J. Reynolds, Visual-induced excitation leads to firing pauses in striatal cholinergic interneurons. *J. Neurosci.* **31**, 11133–43 (2011).
18. G. Morris, D. Arkadir, A. Nevet, E. Vaadia, H. Bergman, Coincident but distinct messages of midbrain dopamine and striatal tonically active neurons. *Neuron*. **43**, 133–43 (2004).
19. Y. Cai, C. P. Ford, Dopamine Cells Differentially Regulate Striatal Cholinergic Transmission across Regions through Corelease of Dopamine and Glutamate. *Cell Rep.* **25**, 3148--3157.e3 (2018).
20. C. Straub, N. X. Tritsch, N. A. Hagan, C. Gu, B. L. Sabatini, Multiphasic modulation of cholinergic interneurons by nigrostriatal afferents. *J. Neurosci.* **34**, 8557–69 (2014).
21. H. T. Chang, Dopamine-acetylcholine interaction in the rat striatum: a dual-labeling

immunocytochemical study. *Brain Res. Bull.* **21**, 295–304 (1988).

22. D. B. Pereira, Y. Schmitz, J. Mészáros, P. Merchant, G. Hu, S. Li, A. Henke, J. E. Lizardi-Ortiz, R. J. Karpowicz, T. J. Morgenstern, M. S. Sonders, E. Kanter, P. C. Rodriguez, E. V Mosharov, D. Sames, D. Sulzer, Fluorescent false neurotransmitter reveals functionally silent dopamine vesicle clusters in the striatum. *Nat. Neurosci.* **19**, 578–586 (2016).
23. E. R. Decker, J. A. Dani, Calcium permeability of the nicotinic acetylcholine receptor: the single-channel calcium influx is significant. *J. Neurosci.* **10**, 3413–20 (1990).
24. R. G. Held, C. Liu, K. Ma, A. M. Ramsey, T. B. Tarr, G. De Nola, S. S. H. Wang, J. Wang, A. M. J. M. van den Maagdenberg, T. Schneider, J. Sun, T. A. Blanpied, P. S. Kaeser, Synapse and Active Zone Assembly in the Absence of Presynaptic Ca2+ Channels and Ca2+ Entry. *Neuron*. **107**, 667-683.e9 (2020).
25. J. Yang, Y. Xiao, L. Li, Q. He, M. Li, Y. Shu, Biophysical Properties of Somatic and Axonal Voltage-Gated Sodium Channels in Midbrain Dopaminergic Neurons. *Front. Cell. Neurosci.* **13**, 317 (2019).
26. A. Ritzau-Jost, T. Tsintsadze, M. Krueger, J. Ader, I. Bechmann, J. Eilers, B. Barbour, S. M. Smith, S. Hallermann, Large, Stable Spikes Exhibit Differential Broadening in Excitatory and Inhibitory Neocortical Boutons. *Cell Rep.* **34**, 108612 (2021).
27. M. Howe, I. Ridouh, A. L. Allegra Mascaro, A. Larios, M. Azcorra, D. A. Dombeck, Coordination of rapid cholinergic and dopaminergic signaling in striatum during spontaneous movement. *Elife*. **8** (2019), doi:10.7554/eLife.44903.
28. P. D. Dodson, J. K. Dreyer, K. A. Jennings, E. C. J. Syed, R. Wade-Martins, S. J. Cragg, J. P. Bolam, P. J. Magill, Representation of spontaneous movement by dopaminergic neurons is cell-type selective and disrupted in parkinsonism. *Proc. Natl. Acad. Sci.* **113**, E2180--E2188 (2016).
29. S. Kaneko, T. Hikida, D. Watanabe, H. Ichinose, T. Nagatsu, R. J. Kreitman, I. Pastan, S. Nakanishi, Synaptic Integration Mediated by Striatal Cholinergic Interneurons in Basal Ganglia Function. *Science*. **289**, 633–637 (2000).

30. M. W. Howe, D. A. Dombeck, Rapid signalling in distinct dopaminergic axons during locomotion and reward. *Nature*. **535**, 505–510 (2016).

31. J. A. da Silva, F. Tecuapetla, V. Paixao, R. M. Costa, Dopamine neuron activity before action initiation gates and invigorates future movements. *Nature*. **554**, 244–248 (2018).

32. T. Dugladze, D. Schmitz, M. A. Whittington, I. Vida, T. Gloveli, Segregation of Axonal and Somatic Activity During Fast Network Oscillations. *Science*. **336**, 1458–1461 (2012).

33. M. E. J. Sheffield, T. K. Best, B. D. Mensh, W. L. Kath, N. Spruston, Slow integration leads to persistent action potential firing in distal axons of coupled interneurons. *Nat. Neurosci.* **14**, 200–207 (2011).

34. J. A. Dani, D. Bertrand, Nicotinic acetylcholine receptors and nicotinic cholinergic mechanisms of the central nervous system. *Annu. Rev. Pharmacol. Toxicol.* **47**, 699–729 (2007).

35. N. Eshel, J. Tian, M. Bukwich, N. Uchida, Dopamine neurons share common response function for reward prediction error. *Nat. Neurosci.* **19**, 479–486 (2016).

36. J. G. Parker, L. S. Zweifel, J. J. Clark, S. B. Evans, P. E. M. Phillips, R. D. Palmiter, Absence of NMDA receptors in dopamine neurons attenuates dopamine release but not conditioned approach during Pavlovian conditioning. *Proc. Natl. Acad. Sci.* **107**, 13491–13496 (2010).

37. A. A. Grace, B. S. Bunney, Nigral dopamine neurons: intracellular recording and identification with L-dopa injection and histofluorescence. *Science*. **210**, 654–6 (1980).

38. L. J. Gentet, S. R. Williams, Dopamine gates action potential backpropagation in midbrain dopaminergic neurons. *J. Neurosci.* **27**, 1892–901 (2007).

39. N. F. Parker, C. M. Cameron, J. P. Taliaferro, J. Lee, J. Y. Choi, T. J. Davidson, N. D. Daw, I. B. Witten, Reward and choice encoding in terminals of midbrain dopamine neurons depends on striatal target. *Nat. Neurosci.* **19**, 845–854 (2016).

40. C. Liu, Data table for an action potential initiation mechanism in distal axons for the control of dopamine release. *Zenodo* (2022); doi:10.5281/zenodo.6342359.

41. C. Liu, Matlab script for object recognition and analysis. *Zenodo* (2022);

doi:10.5281/zenodo.6342367.

42. C. M. Backman, N. Malik, Y. Zhang, L. Shan, A. Grinberg, B. J. Hoffer, H. Westphal, A. C. Tomac, Characterization of a mouse strain expressing Cre recombinase from the 3' untranslated region of the dopamine transporter locus. *Genesis*. **44**, 383–390 (2006).

43. J. Rossi, N. Balthasar, D. Olson, M. Scott, E. Berglund, C. E. Lee, M. J. Choi, D. Lauzon, B. B. Lowell, J. K. Elmquist, Melanocortin-4 Receptors Expressed by Cholinergic Neurons Regulate Energy Balance and Glucose Homeostasis. *Cell Metab.* **13**, 195–204 (2011).

44. L. Madisen, T. Mao, H. Koch, J. Zhuo, A. Berenyi, S. Fujisawa, Y.-W. a Hsu, A. J. Garcia, X. Gu, S. Zanella, J. Kidney, H. Gu, Y. Mao, B. M. Hooks, E. S. Boyden, G. Buzsáki, J. M. Ramirez, A. R. Jones, K. Svoboda, X. Han, E. E. Turner, H. Zeng, A toolbox of Cre-dependent optogenetic transgenic mice for light-induced activation and silencing. *Nat. Neurosci.* **15**, 793–802 (2012).

45. B. Todorov, R. C. G. van de Ven, S. Kaja, L. A. M. Broos, S. J. Verbeek, J. J. Plomp, M. D. Ferrari, R. R. Frants, A. M. J. M. van den Maagdenberg, Conditional inactivation of the Cacna1a gene in transgenic mice. *Genesis*. **44**, 589–94 (2006).

46. A. Pereverzev, M. Mikhna, R. Vajna, C. Gissel, M. Henry, M. Weiergräber, J. Hescheler, N. Smyth, T. Schneider, Disturbances in glucose-tolerance, insulin-release, and stress-induced hyperglycemia upon disruption of the Ca(v)2.3 (alpha 1E) subunit of voltage-gated Ca(2+) channels. *Mol. Endocrinol.* **16**, 884–95 (2002).

47. M. G. L. Gustafsson, L. Shao, P. M. Carlton, C. J. R. Wang, I. N. Golubovskaya, W. Z. Cande, D. A. Agard, J. W. Sedat, Three-dimensional resolution doubling in wide-field fluorescence microscopy by structured illumination. *Biophys. J.* **94**, 4957–4970 (2008).

48. A. Mathis, P. Mamidanna, K. M. Cury, T. Abe, V. N. Murthy, M. W. Mathis, M. Bethge, DeepLabCut: markerless pose estimation of user-defined body parts with deep learning. *Nat. Neurosci.* **21**, 1281–1289 (2018).